Available online at www.sciencedirect.com
ScienceDirect
Icarus 193 (2008) 125–138
ICARUS
www.elsevier.com/locate/icarus

Radio occultation measurements and MGCM simulations of Kelvin waves on Mars

D.P. Hinson [a,*], M. Pätzold [b], R.J. Wilson [c], B. Häusler [d], S. Tellmann [b], G.L. Tyler [a]

[a] *Department of Electrical Engineering, Stanford University, Stanford, CA 94305, USA*
[b] *Institut für Geophysik und Meteorologie, Universität zu Köln, Cologne, Germany*
[c] *NOAA/Geophysical Fluid Dynamics Laboratory, Princeton University, Princeton, NJ 08542, USA*
[d] *Institut für Raumfahrttechnik, Universität der Bundeswehr München, Neubiberg, Germany*

Received 11 May 2007; revised 16 August 2007

Available online 3 October 2007

Abstract

We have derived new results concerning thermal tides on Mars from a combination of radio occultation measurements and numerical simulations by a Mars General Circulation Model (MGCM). This investigation exploits a set of concurrent observations by Mars Express (MEX) and Mars Global Surveyor (MGS) in mid-2004, when the season on Mars was midspring in the northern hemisphere. The MEX occultations sampled the atmosphere near the evening terminator at latitudes ranging from 54° N to 15° S. The MGS occultations provided complementary coverage near the morning terminator at latitudes of 35° N and 71° S. The geopotential field derived from these measurements contains distinctive modulation caused by solar-asynchronous thermal tides. Through careful analysis of the combined observations, we characterized two prominent wave modes, obtaining direct solutions for some properties, such as the amplitude and phase, as well as constraints on others, such as the period, zonal wave number, and meridional structure. We supplemented these observations with MGCM simulations. After evaluating the performance of the MGCM against the measurements, we used the validated simulation to deduce the identity of the two tidal modes and to explore their behavior. One mode is a semidiurnal Kelvin wave with a zonal wave number of 2 (SK2), while the other is a diurnal Kelvin wave with a zonal wave number of 1 (DK1). Both modes are known to be close to resonance in the martian atmosphere. Our observations of the SK2 are more complete and less ambiguous than any previous measurement. The well-known DK1 is the dominant solar-asynchronous tide in the martian atmosphere, and our results confirm and extend previous observations by diverse instruments.

Keywords: Mars, atmosphere; Atmospheres, dynamics

1. Introduction

Solar heating of the martian surface and atmosphere excites an assortment of global-scale atmospheric waves known as thermal tides (e.g., Zurek et al., 1992; Wilson and Hamilton, 1996). The direct response of the atmosphere to solar forcing takes the form of classical modes that are phase locked to the Sun, but the spectrum of tides on Mars includes important contributions from many modes that do not follow the Sun's apparent westward motion. These solar-asynchronous modes arise indirectly through modulation of the solar-locked tides by zonally varying topography and surface thermal properties (e.g., Zurek, 1976; Conrath, 1976; Wilson and Hamilton, 1996) and through nonlinear interactions (e.g., Angelats i Coll et al., 2004).

Martian thermal tides have been observed by a variety of techniques both at fixed locations on the surface and from orbiting satellites. The foundation for current understanding of the solar-locked tides comes from the Viking Landers, which amassed an invaluable record of surface pressure during several martian years of operations. These data have supported numerous investigations of the diurnal and semidiurnal solar-locked modes, allowing characterizations of their general behavior, seasonal evolution, and response to global dust storms (e.g., Leovy, 1981; Zurek and Leovy, 1981; Zurek et al., 1992; Wilson

* Corresponding author. Fax: +1 (650) 723 9251.
E-mail address: dhinson@stanford.edu (D.P. Hinson).

0019-1035/$ – see front matter
doi:10.1016/j.icarus.2007.09.009

and Hamilton, 1996; Bridger and Murphy, 1998). Mars Global Surveyor (MGS) has extended our understanding of the solar-asynchronous tides by acquiring highly complementary observations with global coverage across a wide range of altitudes. For example, measurements of neutral density at aerobraking altitudes (110–160 km) by the MGS accelerometer have revealed surprisingly strong modulation caused by a combination of solar-asynchronous modes (e.g., Forbes and Hagan, 2000; Wilson, 2002; Withers et al., 2003; Wang et al., 2006). In the lower atmosphere (0–40 km), the global structure and seasonal evolution of several prominent solar-asynchronous modes have been characterized through analysis of extensive temperature measurements by the MGS Thermal Emission Spectrometer (TES) (e.g., Wilson, 2000; Banfield et al., 2000, 2003). We will return to these results in Sections 5.3 and 6.3.

Radio occultation experiments conducted with MGS are an important and underutilized source of information about martian thermal tides. Though lacking in global coverage, these experiments have several unique attributes that complement the capabilities of other instruments. For example, electron density profiles derived from occultation measurements contain distinctive longitude-dependent vertical displacements caused by solar-asynchronous tidal modes (e.g., Bougher et al., 2001; Cahoy et al., 2006). In addition, the occultation experiments sound the lower neutral atmosphere at much finer vertical resolution than the TES, enabling an investigation of nighttime tropical temperature inversions associated with thermal tides (Hinson and Wilson, 2004).

In this paper we derive an improved understanding of thermal tides on Mars through further analysis of radio occultation data. We focus on a set of measurements obtained concurrently with MGS and Mars Express (MEX) in mid-2004, taking advantage of the complementary coverage in latitude and local time by the two spacecraft. Section 2 discusses the implementation of these experiments, the retrieval algorithms, and the coverage in longitude, latitude, and local time of the resulting atmospheric profiles. These profiles include unique measurements of geopotential height on surfaces of constant pressure, which have been exploited previously to investigate baroclinic eddies (Hinson, 2006). The results reported here demonstrate the sensitivity and utility of the measured geopotential field for investigations of thermal tides.

We supplement these observations with numerical simulations by the Mars General Circulation Model (MGCM) of the Geophysical Fluid Dynamics Laboratory (GFDL/NOAA) (Wilson and Hamilton, 1996). Section 3 describes the version of the model used here. Our strategy is to evaluate the performance of the MGCM against the occultation measurements, and then to derive a more complete characterization of selected tidal modes from the validated simulation. When used in this way the MGCM helps circumvent inherent limitations of the data, which are discussed in Sections 2.3 and 4.1.

The combined results derived from the occultation measurements and the MGCM simulation allow clear identification of two solar-asynchronous tidal modes. Both are Kelvin waves, one with a semidiurnal period and a zonal wave number of 2, as discussed in Section 5, and the other with a diurnal period and a zonal wave number of 1, as described in Section 6. These eastward traveling Kelvin waves circle Mars with a zonal phase speed of about 240 m s^{-1} at the equator, moving at the same rate but in the opposite direction as the westward traveling solar-locked tides.

Zurek (1988) investigated the planetary-scale normal modes of the martian atmosphere within an idealized theoretical framework. His calculations indicate that the Kelvin waves identified here are close to resonance, and this conclusion was substantiated by subsequent MGCM simulations (Wilson and Hamilton, 1996). Hence, the lowest-order Kelvin waves are excited efficiently on Mars through resonant amplification of tidal forcing (Zurek, 1988). The first evidence for the diurnal Kelvin wave was obtained from analysis of temperature measurements by the Mariner 9 Infrared Interferometer Spectrometer (Conrath, 1976), and it was later characterized in far greater detail by the MGS TES (Wilson, 2000; Banfield et al., 2003) and the MGS accelerometer (Forbes and Hagan, 2000; Wilson, 2002; Withers et al., 2003). Both the diurnal and semidiurnal Kelvin waves make a significant contribution to the oscillations in surface pressure observed by the Viking Landers (Wilson and Hamilton, 1996; Bridger and Murphy, 1998). This paper demonstrates that the same Kelvin waves are readily identified in radio occultation measurements of geopotential height, which yield valuable new insight.

We close our introductory remarks by defining a few parameters. The areocentric longitude of the Sun, L_s, measures the seasons on Mars, with $L_s \equiv 0°$ at the vernal equinox of the northern hemisphere. In assigning numbers to martian years we adopt the convention that Mars year 1 (MY 1) began at $L_s = 0°$ on 11 April 1955. The term sol denotes the mean solar day of 88,775 s. Each sol is subdivided into 24 true solar hours, and we will refer to these as hours for short.

2. Radio occultation measurements

Radio occultation experiments were conducted routinely with MGS between May 1999 and September 2006, yielding more than 21,000 profiles of the neutral atmosphere (e.g., Hinson et al., 1999; Tyler et al., 2001; Hinson, 2006). MEX began performing radio occultation experiments in April 2004 and has completed several seasons of observations, which will continue as part of an ongoing extended mission (Pätzold et al., 2004). This section describes the main characteristics of these experiments and summarizes the results obtained in mid-2004.

2.1. Equipment

Radio occultation experiments are designed to measure the refractive bending caused by a planetary atmosphere in a limb-sounding geometry. MGS performs these experiments in a simple "one-way" mode of communication, using coherent microwave radiation transmitted by the spacecraft and received at tracking stations of NASA's Deep Space Network (DSN) (Hinson et al., 1999; Tyler et al., 2001). The radio link consists

of a single, unmodulated signal with a frequency of 8.4 GHz (a wavelength of 3.6 cm). The accuracy of these measurements depends critically on frequency stability, and measurements in the one-way mode require stable frequency references at both ends of the radio link. The MGS payload therefore includes a temperature-controlled, ultrastable oscillator (USO) with a fractional frequency stability (Allan deviation) of about 10^{-13} for integration times of 1–1000 s. The DSN receivers are referenced to cryogenic hydrogen masers, with a fractional frequency stability of about 10^{-13} at 1 s, 10^{-14} at 10 s, and 10^{-15} at 100–1000 s.

Unlike MGS, MEX carries no USO. In the absence of a high-stability frequency reference on the spacecraft, MEX conducts its occultation experiments in a "two-way" mode of communication (Pätzold et al., 2004). During the experiments considered here a tracking antenna on Earth transmits an unmodulated signal at a frequency of 7.2 GHz (4.2 cm) to MEX. Using this uplink signal as a frequency reference, MEX generates a pair of coherent downlink signals and transmits them back to the tracking antenna on Earth, where the data are recorded for subsequent processing. The frequency ratios of the signals transmitted and received by MEX are 880/749 and 240/749, resulting in downlink frequencies of 8.4 GHz (3.6 cm) and 2.3 GHz (13.1 cm), respectively. This two-way configuration attains the frequency stability required for high-quality atmospheric sounding by using a single hydrogen maser as the absolute frequency reference for the signals transmitted and received by the tracking station on Earth.

About one third of the MEX occultations were conducted with a recently constructed tracking station of the European Space Agency (ESA) in New Norcia, Australia. The others utilized tracking stations of the NASA DSN, which collected data when Mars was not visible from New Norcia.

2.2. *One-way and two-way retrieval algorithms*

We retrieved atmospheric profiles from both the one-way MGS and the two-way MEX radio occultation data using the standard "Abel-transform" algorithm (e.g., Fjeldbo et al., 1971), which is based on the laws of geometrical optics. Despite important differences in implementation for the one-way and two-way experiments, the fundamental characteristics of the resulting atmospheric profiles are essentially the same.

Within the framework of geometrical optics, a radio signal travels along a narrow "ray path" between the transmitter and the receiver. The ray path curves gradually within the atmosphere of Mars in response to refractive index gradients, causing an angular deflection between the incoming and outgoing rays and a Doppler shift in the frequency of the received signal. Both the deflection and the resulting Doppler shift vary with time as the ray path slices through the atmosphere (e.g., Hinson et al., 1999, Figs. 2 and 3).

The method used to retrieve atmospheric profiles from the MGS occultation data is described by Hinson et al. (1999). We limit discussion here to one key aspect of this procedure that differs for one-way and two-way experiments. In the one-way MGS experiments, the properties of a particular downlink ray—the impact parameter and the amount of refractive bending caused by the atmosphere of Mars—can be determined uniquely from the Doppler shift observed when the corresponding radio signal arrived on Earth. This step requires an accurate reconstruction of the spacecraft trajectory, which is provided by the MGS Navigation Team. Analysis of the complete data from each occultation experiment yields a profile of bending angle versus impact parameter that is the basis for all subsequent steps of profile retrieval.

The situation with the two-way MEX experiments is more complex. The uplink and downlink rays follow slightly different paths through the atmosphere of Mars, so that their minimum altitudes, impact parameters, and angular deflections are not the same. The fundamental observation is now the net Doppler shift resulting from the combined effects of the uplink and downlink segments of the radio link. The distinct properties of the two ray paths cannot be determined uniquely from this single measurement, but a self-consistent solution can be obtained through iteration (cf. Jenkins et al., 1994). In each pass through the data, the difference between the impact parameters of the uplink and downlink rays is required to be consistent with the estimates of refractive bending from the previous pass. This algorithm imposes no artificial constraints, and the solution for the atmospheric profile is guided only by the ephemerides of the spacecraft, Mars, and Earth, which are well known, and the observed Doppler shift.

Each MGS occultation experiment yields a profile of temperature T and pressure p versus planetocentric radius that extends from the surface to a pressure of about 10 Pa, corresponding to an altitude of about 40 km in the tropics. The vertical resolution is diffraction limited to about 0.5 km (Karayel and Hinson, 1997; Hinson et al., 1999). The fractional uncertainties in T and p vary strongly with pressure, decreasing from about 5% at 10 Pa to about 0.3% at 610 Pa, near the surface. The radius scale inherent in each profile has an uncertainty of a few meters, commensurate with the accuracy of the MGS orbit reconstructions (e.g., Lemoine et al., 2001). This allows accurate registration of the retrieved profiles within the gravity field of Mars, providing a unique measure of geopotential height Z on surfaces of constant pressure. The uncertainty in p limits the accuracy of Z to about 30 m at 610 Pa, increasing to about 80 m at 200 Pa.

The profiles retrieved from the MEX occultation experiments have the same characteristics, with two notable exceptions. First, the use of a two-way radio link offers increased sensitivity by doubling the Doppler shift caused by the martian atmosphere. The measurement noise also increases but by a lesser amount, so that the MEX profiles generally extend to smaller pressures, about 5 Pa for the experiments considered here. Second, the vertical resolution of the MEX profiles is determined primarily by the separation in radius between the uplink and downlink rays, which ranged from about 2 km in the initial experiments at northern midlatitudes to about 0.6 km in the final experiments in the southern tropics. These limits to vertical resolution exceed the characteristic Fresnel scale of diffraction effects, which decreased steadily from 1 km to 0.5 km within this set of observations.

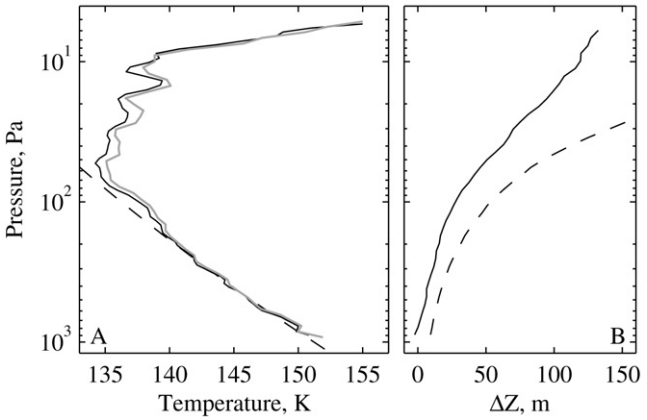

Fig. 1. Results obtained from nearly coincident measurements by MEX and MGS on 23 August 2005. In observations separated by 13 min, the two spacecraft sounded the atmosphere at essentially the same location near the winter pole (70° E, 76° N, $L_s = 274°$). (A) Temperature profiles from MEX (dark line) and MGS (light line) agree to within 1 K and exhibit nearly identical small scale structure. The dashed line is the saturation vapor pressure of CO_2. (B) The difference in geopotential height, ΔZ, between the MEX and MGS profiles (solid line) remains within the standard deviation of the measurements (dashed line).

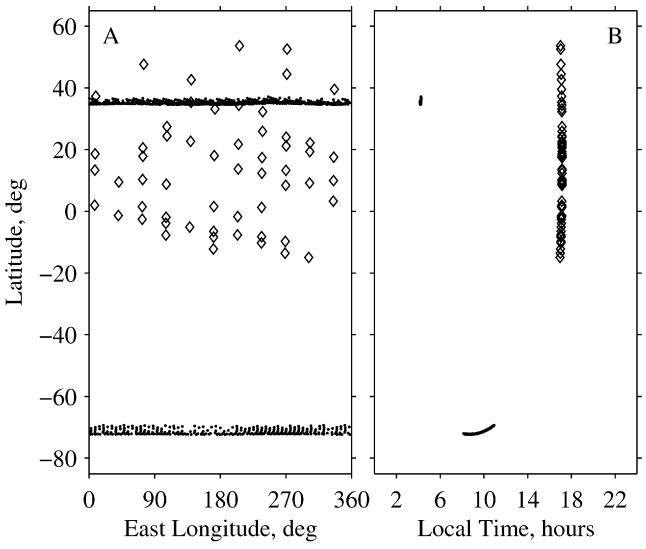

Fig. 2. (A) Areographic locations of radio occultation measurements by MEX (diamonds) and MGS (dots) during mid-2004. (B) Distribution in local time of the same measurements.

It is important to determine whether the one-way and two-way experiments yield consistent results. We address this issue with a direct empirical test. Fig. 1 compares profiles retrieved from nearly coincident radio occultation measurements by MEX and MGS, which occurred by chance on 23 August 2005. These profiles are from 70° E, 76° N, at $L_s = 274°$, near winter solstice of MY 27. For both spacecraft the line of sight to Earth coincided with the north–south direction at the limb of Mars, so that the horizontal resolution was about 5° in latitude. The experiment geometries differed only in the distance between the spacecraft and the limb of Mars, 1800 km for MGS and 11,400 km for MEX. The offsets in longitude (0.4°), latitude (0.06°), local time on Mars (10 min), and time of observation (13 min) are negligible. The temperature profiles agree closely, as shown in Fig. 1A, and the maximum difference of about 1 K at 10–30 Pa is within the measurement uncertainties. The agreement extends to small-scale vertical variations in temperature, which are probably caused by vertically propagating gravity waves. The profiles of geopotential height differ by 16 m at 200 Pa, increasing to 89 m at 20 Pa, but the difference remains smaller than the standard deviation of the measurements, as shown in Fig. 1B. This comparison confirms the accuracy of the basic measurements as well as the consistency of the retrieval algorithms applied to the two sets of observations.

2.3. Spatial and temporal coverage

Radio occultation measurements of the neutral atmosphere of Mars were obtained simultaneously by MEX and MGS during April–August 2004. This series of joint observations extends from the start of routine MEX science operations to solar conjunction. The season on Mars was midspring of the northern hemisphere, $L_s = 35°$–$70°$, near aphelion of MY 27. During this interval, MGS sounded the atmosphere at both occultation entry and exit, while MEX experiments were conducted only at occultation entry. The two spacecraft provide complementary coverage in latitude and local time as a consequence of their dramatically different orbits.

Fig. 2A shows the locations in latitude and longitude of the measurements considered here. The MEX measurements began at northern midlatitudes and drifted steadily southward into the southern tropics, while the MGS measurements remained at essentially fixed latitudes of 35° N (entry) and 71° S (exit). The longitude distribution is determined by the orbital periods of the two spacecraft. MEX completes 11 orbits in 3 sols, which restricts the occultation measurements to 11 discrete longitudes. MGS completes 88 orbits in about 7 sols so that the measurements drift steadily in longitude from sol to sol (e.g., Hinson and Wilson, 2004, Fig. 1a). Over time this results in relatively dense coverage in longitude within restricted ranges of latitude, as shown in Fig. 2A.

Occultation data were not recorded during every geometric opportunity, owing to gaps in tracking coverage by the DSN and ESA antennas. Neither spacecraft is tracked continuously. The resulting gaps in MEX coverage are apparent in Fig. 2A, but the corresponding gaps for MGS are obscured by the large density of samples within two narrow ranges of latitude. During this interval, MGS occultation data were recorded in about 75% of the opportunities for observations.

Each spacecraft sounded the atmosphere at a different range of local times on Mars, as shown in Fig. 2B. The MEX experiments occurred near the evening terminator at local times of 17.0–17.2 h. The MGS experiments at occultation entry provided complementary coverage near the morning terminator at local times of 4.2–4.3 h. The roughly half-sol offset in local time between these two sets of observations provides important leverage for investigating thermal tides. At occultation exit, MGS sampled the polar atmosphere at local times of 8–11 h.

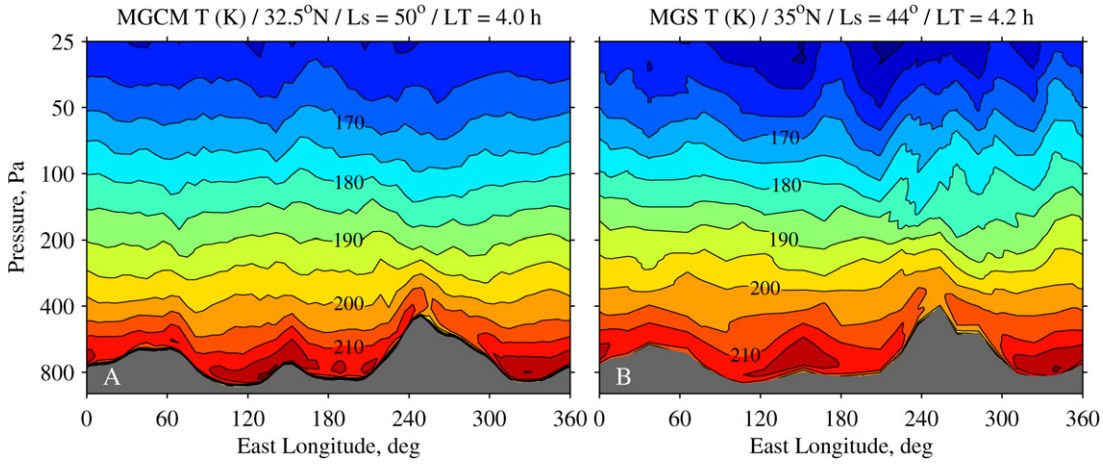

Fig. 3. Thermal structure at fixed latitude and local time from (A) the MGCM simulation (32.5° N, 4 h) and (B) MGS radio occultation measurements (35° N, 4.2 h). The contour interval is 5 K. The surface is shown by gray shading. At this latitude, the highest surface elevations occur near Alba Patera (250° E) and Syrtis Major (60° E).

In summary, the combined MGS and MEX observations provide much better coverage in latitude and local time than either set alone.

3. The GFDL Mars General Circulation Model

The GFDL MGCM was introduced by Wilson and Hamilton (1996) just prior to the launch of MGS in November 1996. Extensive observations by MGS during the following decade enabled further development of the MGCM by providing a greatly improved characterization of Mars and its atmosphere. For example, definitive maps of both surface topography (Smith et al., 2001) and surface thermal inertia (Putzig et al., 2005) are now available as boundary conditions for the MGCM. Atmospheric aerosols are key determinants of martian climate, and recent measurements of their basic properties (Clancy et al., 2003; Wolff and Clancy, 2003) along with their spatial and seasonal distributions (Smith, 2004) provide important constraints for numerical modeling of radiative transfer. In addition, the MGCM has been refined and validated through direct comparisons of model predictions with MGS measurements of large-scale atmospheric disturbances, such as thermal tides (Wilson, 2000, 2002; Banfield et al., 2003; Hinson and Wilson, 2004) and traveling waves that arise from instabilities (Hinson and Wilson, 2002; Wilson et al., 2002; Wang et al., 2003).

We used a version of the MGCM with the following characteristics. The horizontal resolution is 5° in latitude by 6° in longitude. The vertical grid consists of 22 levels extending from the surface to an altitude of about 90 km. The radiative effects of dust are modeled in the manner described by Hinson and Wilson (2004), but the radiative effects of water ice clouds are ignored. In the simulation used here, the horizontal distribution of dust and its time variations are prescribed by requiring the column opacity to match measurements by the MGS TES (Smith, 2004). The model for the vertical distribution of dust resembles the one used by Montmesin et al. (2004, Fig. 1), with some adjustments that result in closer agreement between the simulated and observed zonal mean temperature fields.

Fig. 3 compares the temperature field from the MGCM simulation with results from MGS radio occultations. Both panels show longitude-height cross sections at fixed latitude and local time. The simulated temperature field is the average from a 10-sol interval centered on $L_s = 50°$. The measured temperature field was constructed from 23 profiles collected on 6–7 June 2004 at $L_s = 44°$. The resolution in longitude of these measurements is about 15°, as compared with 6° for the simulation.

The measurements in Fig. 3B generally confirm the accuracy of the simulation in Fig. 3A. The zonally averaged temperatures are essentially the same throughout this pressure range. There are notable similarities between the simulation and the measurements at pressures greater than 400 Pa, where the surface topography imposes strong zonal modulation on the temperature field. We will return to this simulation in Sections 5.2 and 6.2, where other aspects of its performance will be tested against observations by both MGS and MEX.

4. Space–time analysis of atmospheric waves

We identify and characterize atmospheric waves through least squares analysis of radio occultation data using the same general approach described previously by Hinson (2006). Section 4.1 introduces a simple wave model and explains the information content of the data considered here. Section 4.2 presents initial results from least squares analysis, which motivate the focused investigations that follow in Sections 5 and 6.

4.1. Basic wave model

We are interested primarily in longitude-time variations of geopotential height at constant pressure and latitude. Our model for these variations includes contributions from two sources:

$$\hat{Z} \equiv \overline{Z}(L_s) + Z'(\lambda, t_U). \quad (1)$$

The first term $\overline{Z}$ represents the gradual seasonal trend and depends primarily on L_s (cf. Hinson, 2006, Fig. 1a). The sec-

ond term Z' represents the effects of global scale atmospheric waves, which vary sinusoidally with east longitude λ and universal time t_U:

$$Z'(\lambda, t_U) \equiv \sum A \cos(s\lambda - 2\pi\sigma t_U - \psi). \quad (2)$$

An atmospheric wave is identified by its frequency σ, zonal wave number s, amplitude A, and phase ψ. In the notation used here s is a dimensionless integer and σ is expressed in cycles sol^{-1}. We adopt the convention that $s \geqslant 0$, so that positive and negative values of σ correspond to waves traveling eastward and westward, respectively. The summation reflects the possible presence of several distinct atmospheric waves.

The wave model in Eq. (2) involves no assumptions about variations with pressure or latitude. We will construct an empirical description of the vertical and meridional structure of a particular s–σ mode by solving for A and ψ at each pressure level and latitude interval where data are available (cf. Banfield et al., 2003). The solutions for A and ψ are free to vary with pressure and latitude.

The sampling of our observations in local time is restricted to a few discrete values, as shown in Fig. 2B. This is a consequence of the systematic dependence of the measurement longitude λ on the time of observation t_U:

$$t_U + \lambda/\Omega \approx t_L \approx \text{constant}. \quad (3)$$

Here, t_L is the local true solar time and Ω is the effective rotation rate of 2π sol^{-1}. We can illustrate the implications of this dependence on our wave measurements by combining (2) and (3):

$$Z'(\lambda, t_L) = \sum A \cos\big[(s + \sigma T)\lambda - 2\pi\sigma t_L - \psi\big], \quad (4)$$

where $T = 2\pi/\Omega$ is the mean solar day. Equation (2) expresses the wave structure within a coordinate frame attached to Mars, while Eq. (4) is more convenient for interpreting observations from an orbiting satellite.

Observations at fixed t_L provide a direct measure of

$$f \equiv |\sigma + s/T|, \quad (5)$$

the Doppler shifted frequency as observed in the satellite frame (Conrath, 1981; Lait and Stanford, 1988). A solution for f constrains the values of s and σ but does not define them uniquely. For example, an eastward traveling, wave-1, diurnal tide ($s = 1$, $\sigma = 1$ sol^{-1}) yields the same fundamental frequency, $f = 2$ sol^{-1}, as a stationary wave-2 disturbance ($s = 2$, $\sigma = 0$ sol^{-1}) or a zonally symmetric semidiurnal oscillation ($s = 0$, $\sigma = 2$ sol^{-1}). Moreover, $f \equiv 0$ sol^{-1} for all solar-locked thermal tides, which are therefore independent of λ when viewed at fixed local time. We restrict attention in this paper to thermal tides and stationary waves, so that s, σ, and f are integers.

From Eq. (4), the maximum of Z' associated with a particular atmospheric wave occurs at longitude

$$\lambda_m = \frac{2\pi\sigma t_L + \psi}{s + \sigma T}. \quad (6)$$

With this notation Eq. (4) becomes

$$Z'(\lambda, t_L) = \sum A \cos\big[fT(\lambda - \lambda_m)\big], \quad (7)$$

where the dependence of Z' on t_L is implicit in λ_m. Owing to the periodicity of Z', λ_m is ambiguous by integer multiples of $2\pi/(fT)$.

Measurements at two or more well-separated local times provide additional constraints on the values of s and σ (e.g., Chapman et al., 1974; Banfield et al., 2000, 2003), and elegant methods of space-time analysis have been developed to extract this information (e.g., Salby, 1982; Lait and Stanford, 1988). In this paper we simply use the measurements to characterize the variation of λ_m with t_L, yielding the following constraint:

$$\frac{d\lambda_m}{dt_L} = \frac{2\pi\sigma}{s + \sigma T}. \quad (8)$$

Solutions for both s and σ can then be obtained by combining this result with the previous measurement of f. The limitations of this approach are discussed further in Section 5.1.

Throughout this section we have expressed λ and λ_m in radians, but in reporting results it is more convenient to use degrees of longitude.

4.2. Measured spectra

Several prominent wave modes appear in the measurements considered here, and these can be readily identified through spectral analysis. In our initial survey of the data, we relied primarily on the MGS measurements, which occur more frequently than MEX observations and are less susceptible to aliasing.

We conducted an initial assessment of the data at the 200-Pa pressure level. One sample of Z was obtained from each retrieved profile through interpolation. Within a subset of data spanning 22 sols at $L_s = 50°$–$60°$, we solved for the seasonal trend $\overline{Z}$ by fitting a quadratic polynomial to samples of Z versus L_s. We then systematically compared the wave model Z' with the detrended observations, $Z - \overline{Z}$, obtaining least squares solutions for A and λ_m for a range of possible values of f. The presence of one or more atmospheric waves is reflected by a strong correlation between the wave model and the observations for discrete values of f, resulting in relatively large values for A.

Fig. 4 shows results derived from MGS measurements at both 35° N and 72° S. Each panel contains a power spectrum constructed from least squares analysis. Results are shown for $0 < f < 6.3$ sol^{-1}. This frequency range is constrained by the effect of aliasing on the MGS measurements, which have a sample spacing of about 0.08 sols in time of observation (about 29° in λ). Any signals with $f > 6.3$ sol^{-1} are aliased into this range.

The spectra in Fig. 4 contain prominent peaks precisely at integer values of f. Multiple waves appear at 35° N, producing strong modulation at 1, 2, and 4 sol^{-1}, while wave activity at 1 sol^{-1} dominates the spectrum at 72° S. Given that s must be an integer, this implies that σ is also an integer. The spectral peaks therefore arise from some combination of stationary waves ($\sigma = 0$ sol^{-1}) and thermal tides ($\sigma = \pm1, \pm2, \ldots$ sol^{-1}). Moreover, the oscillations of Z must be very regular to produce such narrow spectral peaks. The width of the strongest

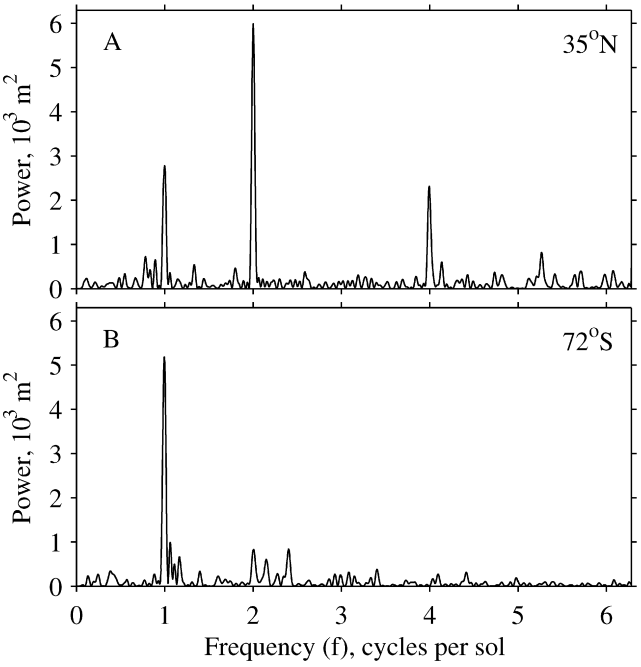

Fig. 4. Spectra of geopotential height from MGS measurements at (A) 35° N and (B) 72° S. These results are from the 200-Pa pressure level during $L_s = 50°$–$60°$ of MY 27. In these observations the frequency of an atmospheric wave is Doppler shifted by the rotation of Mars, as expressed by Eq. (5), so that the spectra measure the combined effects of zonal and temporal variations.

peaks corresponds to the spectral resolution of the measurements, about 0.05 sol^{-1} for a data span of 22 sols.

A strong wave-1 stationary Rossby wave ($s = 1$, $\sigma = 0$ sol^{-1}, $f = 1$ sol^{-1}) was observed by the MGS TES during the same season of MY 24 (Banfield et al., 2003, Fig. 9). The wave is excited through topographic modulation of a seasonal jet in the zonal wind field at middle-to-high southern latitudes, and these winds confine the wave activity to the same latitude range (Banfield et al., 2003, Fig. 3). This stationary wave is almost certainly responsible for the prominent $f = 1$ sol^{-1} feature at 72° S in Fig. 4B (see also Wilson, 2000; Hinson et al., 2003). The origin of the $f = 1$ sol^{-1} feature at 35° N in Fig. 4A is far less clear, and it may include contributions from both stationary waves and thermal tides.

The wave modes in Fig. 4 at $f = 2$ and 4 sol^{-1} are quite strong at 35° N but insignificant at 72° S. This contrasts with the observed behavior of planetary-scale stationary waves at this season, where the peak amplitude occurs at high southern latitudes in the vicinity of the winter polar jet (Wilson, 2000; Banfield et al., 2003). Thermal tides therefore offer the most plausible explanation for these features. We present a detailed investigation of the wave activity at $f = 2$ and 4 sol^{-1} in the sections that follow. From a combination of data analysis and MGCM simulation, we will show that tidal Kelvin waves are the source of both spectral features.

5. The semidiurnal Kelvin wave

In this section we focus on the spectral feature at $f = 4$ sol^{-1} in Fig. 4A. We begin by deriving basic properties of the wave through analysis of measurements by MEX and MGS. A comparison of the MGCM simulation with this empirical description then yields a more complete and specific classification of the wave.

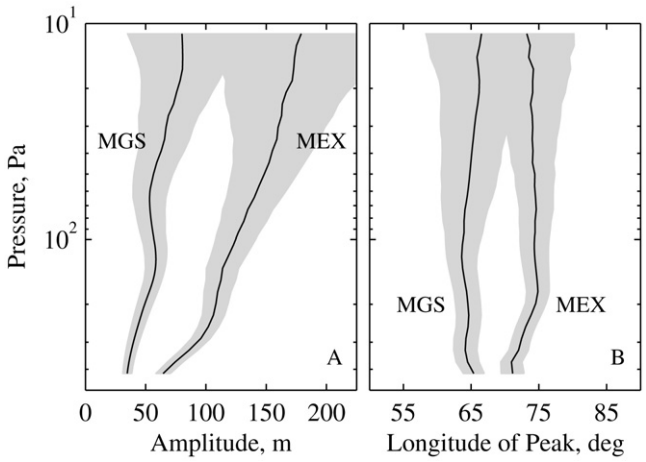

Fig. 5. Structure of the $f = 4$ sol^{-1} wave mode as derived from measurements of geopotential height by MGS and MEX. The dark lines show least squares solutions for (A) the amplitude A and (B) the longitude of maximum geopotential λ_m. The standard deviations are denoted by gray shading. The MGS measurements are at latitude 35° N and local time 4.2 h. The MEX measurements are closer to the equator, centered at 10° N, and roughly half a day later in local time at 17.1 h.

5.1. Observations

Activity at $f = 4$ sol^{-1} is absent from high southern latitudes, so we considered only the low-latitude measurements acquired at occultation entry. We selected two subsets of data for detailed analysis. The first set consists of 327 MGS entry profiles obtained during $L_s = 47°$–$63°$ at fixed local time (4.2 h) and fixed latitude (35° N). The second set comprises 38 MEX entry profiles obtained concurrently at fixed local time (17.1 h) within the tropics (26° N–8° S).

Each subset of data was analyzed separately using the procedure described in Section 4.2. We considered a set of pressure levels with a uniform spacing of $H/8$, where H is the pressure scale height. At each pressure level, we obtained least squares solutions for the wave amplitude A and the longitude of peak geopotential λ_m subject to the constraint that $f = 4$ sol^{-1}. Fig. 5 shows the results derived independently from the two subsets of observations. Note that we have restricted the analysis to pressures less than 400 Pa. At greater pressures, the atmospheric structure is strongly modulated by large zonal variations of topography (see Fig. 3), and the measurements are more difficult to interpret.

According to the MGS and MEX measurements in Fig. 5, the $f = 4$ sol^{-1} mode has the following characteristics. The phase λ_m is essentially independent of height in both sets of measurements, as shown in Fig. 5B. The absence of appreciable phase tilt in the vertical implies that the wave propagates zonally but not vertically, consistent with the behavior expected for a global normal mode or "edge wave" (Andrews et al., 1987, Section 4.4). Although the shift in λ_m between the two local

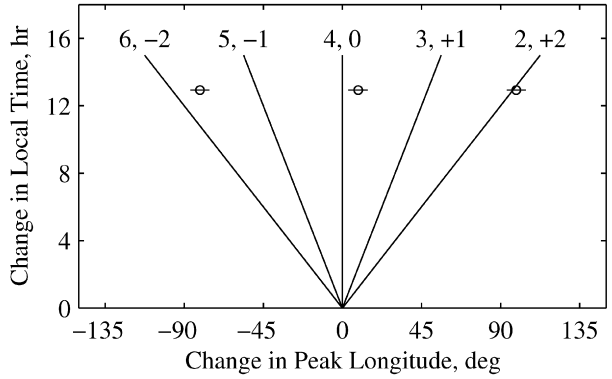

Fig. 6. Variation of λ_m with t_L for the $f = 4$ sol^{-1} wave mode. The circles show results derived from the MGS and MEX observations, as expressed by Eq. (9), with horizontal bars that indicate the standard deviation of the combined measurements. The set of five lines shows the predictions of the simple wave model in Eq. (8). The numbers adjacent to each line indicate the assumed values of s and σ, respectively, with the latter expressed in sol^{-1}. Each combination yields $f = 4$ sol^{-1}.

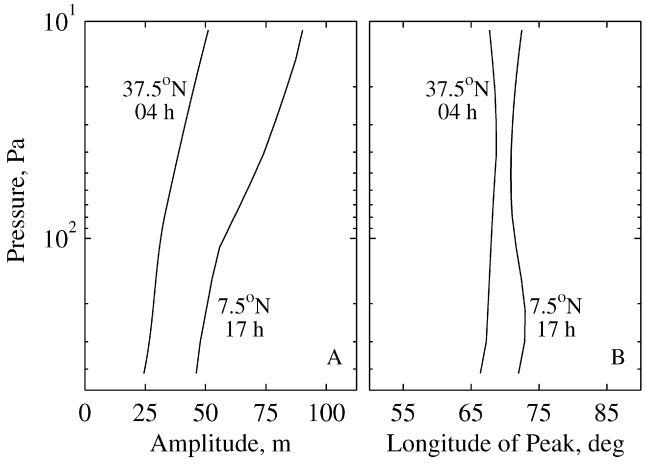

Fig. 7. Structure of the dominant $f = 4$ sol^{-1} wave mode ($s = 2$, $\sigma = 2$ sol^{-1}) in the MGCM simulation at $L_s = 50°$. The two panels show vertical profiles of (A) A and (B) λ_m as simulated by the MGCM at essentially the same latitudes and local times as the observations in Fig. 5. The amplitude scales used here and in Fig. 5 differ by a factor of 2, but the displays are otherwise the same.

times is small, about 9° of longitude, it exceeds the formal uncertainties at pressures greater than 40 Pa. The amplitude generally grows with increasing height, as shown in Fig. 5A, though at a distinctly slower rate than expected for a vertically propagating wave. This implies that the corresponding energy density decays with height, and this property is again consistent with the behavior of a vertically evanescent edge wave. Finally, the amplitude is larger by a factor of about 2 in the MEX measurements, which are closer to the equator. For example, the amplitudes observed by MGS and MEX at the 200 Pa pressure level are 50 ± 6 m and 108 ± 10 m, respectively.

When the profiles of λ_m in Fig. 5B are averaged over pressure, we obtain mean values $\overline{\lambda_m}$ of 65° E at local time 4.2 h (MGS) and 74° E at local time 17.1 h (MEX). As noted previously in connection with Eq. (7), these solutions for $\overline{\lambda_m}$ are ambiguous by integer multiples of $\pi/2$ radians or 90° of longitude when $fT = 4$. The change in $\overline{\lambda_m}$ that occurs in the 12.9 h interval in local time between the MGS and MEX observations is therefore

$$\overline{\lambda_m}(17.1\text{ h}) - \overline{\lambda_m}(4.2\text{ h}) = 9° + n \times 90°, \quad (9)$$

where n is any integer. This constraint on the variation of $\overline{\lambda_m}$ with t_L is shown in Fig. 6.

We interpreted this result through use of Eq. (8). Fig. 6 shows model predictions for $d\lambda_m/dt_L$ for several possible combinations of s and σ when $fT = 4$. On the basis of this comparison we can immediately reject the two diurnal modes ($\sigma = \pm 1$ sol^{-1}). Among the remaining possibilities, the mode that best fits the observations is an eastward traveling, wave-2, semidiurnal tide ($s = 2, \sigma = 2$ sol^{-1}). We are able to distinguish among the semidiurnal and stationary modes only because the change in local time between the MGS and MEX observations differs appreciably from 12 h.

5.2. MGCM simulations

In Fig. 3 we showed that the simulated temperature field compares favorably with MGS observations. The results in Figs. 5 and 6 now provide more challenging benchmarks for evaluating the performance of the MGCM.

We used space-time Fourier analysis to identify and characterize the atmospheric waves that appear in the MGCM simulation at $L_s = 50°$, focusing on the geopotential field at middle-to-low latitudes and pressures greater than 10 Pa. Among the combinations of s and σ that yield $f = 4$ sol^{-1}, such as those noted in Fig. 6, we found only two waves with significant amplitude within these ranges of pressure and latitude. One is an eastward-traveling, wave-2, semidiurnal tide ($s = 2$, $\sigma = 2$ sol^{-1}), while the other is an eastward-traveling, wave-3, diurnal tide ($s = 3$, $\sigma = 1$ sol^{-1}). The former is consistent with the results in Fig. 6, and it also has a larger amplitude at the location of these measurements, which make it a good candidate for explaining the observations. For future reference, the latter is a vertically propagating, diurnal, wave-3, Kelvin wave (DK3). The DK3 has appeared previously in MGCM simulations (Wilson, 2000; Angelats i Coll et al., 2004), but unambiguous observations are not yet available (see Section 5.3).

We extracted the amplitude and phase of the geopotential field for the $s = 2$, $\sigma = 2$ sol^{-1} wave mode in the MGCM simulation. Fig. 7 shows the results at essentially the same latitudes and local times as the measurements in Fig. 5. The simulation matches several general features of the observations: (i) the phase is essentially independent of height, (ii) the amplitude is larger near the equator, and (iii) the amplitude grows with increasing height, but at a rate much slower than expected for a vertically propagating wave. Comparison of Figs. 5B and 7B also shows that the absolute phase of the simulated wave is within a few degrees of the value observed at both local times throughout this pressure range. There is one significant discrepancy in that the simulated wave amplitude is too weak by about a factor of 2. Nonetheless, the simulation captures the main features of the observed wave, and we can now use it to deduce the wave's identity and global structure.

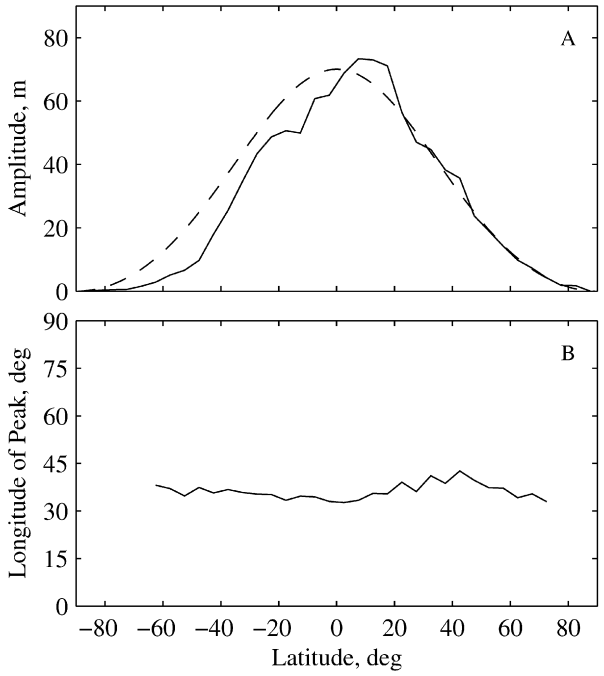

Fig. 8. Numerical models for wave structure at the 43-Pa pressure level. The solid lines show (A) the amplitude in geopotential height and (B) the longitude of the peak in geopotential for the eastward-propagating, wave-2, semidiurnal tide in the MGCM simulation at $L_s = 50°$. The phase is shown at a local time of 0 h over the latitude range where the amplitude exceeds 2 m. The dashed line in the upper panel shows the meridional structure predicted by Laplace's tidal equations for a semidiurnal, wave-2, Kelvin wave.

Fig. 8 shows the meridional structure of this wave as simulated by the MGCM at 43 Pa, about 25 km above the surface. The wave amplitude is largest near the equator and generally decreases with increasing latitude in both hemispheres, with approximate symmetry about the equator. In these respects the mode has the appearance of a Kelvin wave (e.g., Andrews et al., 1987, Section 4.7.1). This meridional structure results in a very small amplitude at 72° S, consistent with the measurements in Fig. 4B. There is little variation of phase with latitude, as shown in Fig. 8B. At 0 h local time, the peak in the simulated geopotential field occurs at an average longitude of 36° E.

We tested our classification of the wave within the framework of Laplace's tidal equations (LTE), which model the behavior of small-amplitude waves in a resting spherical atmosphere (e.g., Andrews et al., 1987, Section 4.2). Fig. 8A compares the results from the MGCM with the meridional structure predicted by LTE for a semidiurnal, wave-2, Kelvin wave (SK2). The similarities in overall structure and meridional scale provide further confirmation of the wave's identity. Although wind shear is neglected in the LTE formulation, its predictions remain reasonably accurate in this case. This is due in part to the relatively large zonal phase speed of the SK2, about 240 m s^{-1} at the equator, which reduces its sensitivity to wind shear.

5.3. Discussion

Few other observations of the SK2 are currently available. The new results derived here bridge the gap between previous measurements at the surface by the Viking Landers and a possible detection at aerobraking altitudes (110–160 km) by the MGS accelerometer.

Wilson and Hamilton (1996) previously used the GFDL MGCM in its pre-MGS configuration to investigate the behavior of thermal tides on Mars, with emphasis on understanding variations in surface pressure observed by the Viking Landers. We focus initially on their simulations of the semidiurnal tide and defer discussion of the diurnal tide to Section 6.3. Wilson and Hamilton (1996) found that the semidiurnal oscillations of surface pressure $S_2(p)$ result primarily from the classical solar-locked semidiurnal tide ($s = 2$, $\sigma = -2$ sol^{-1}). In addition, $S_2(p)$ contains an important contribution from the nearly resonant SK2. Interference between these westward and eastward traveling waves produces zonal modulation in the amplitude and phase of $S_2(p)$, including a standing wave (Wilson and Hamilton, 1996, Fig. 9b). According to the MGCM, $S_2(p)$ evolves in response to seasonal changes in the relative amplitude of the two wave modes. The strongest interference occurs around northern summer solstice when the SK2 intensifies and the amplitudes of the two waves are comparable (Wilson and Hamilton, 1996, Fig. 10 and Table 2; Bridger and Murphy, 1998, Fig. 3a). This enhancement of the SK2 near northern summer solstice causes a distinctive delay in the phase of $S_2(p)$ at the location of both Viking Landers. In this regard, similarities between the model predictions and the Viking Lander observations provide indirect but convincing evidence for the presence of the SK2 in the martian atmosphere.

Radio occultation measurements provide a distinctly different view of thermal tides than the Viking Landers. As noted previously in connection with Eqs. (4) and (5), the solar-locked tides are independent of longitude when viewed at fixed local time. Satellites in polar orbit can therefore observe the SK2 without interference from the semidiurnal solar-locked component. This allows the SK2 to be identified clearly in measurements with sufficient sensitivity and suitable sampling in longitude and local time, as shown in Figs. 4–6. The results in those figures represent the most direct observations to date of the SK2 in the lower atmosphere and the first measurements of its vertical structure in that region.

Wave modes with evanescent vertical structure or large vertical wavelengths tend to be more prominent in geopotential height than in temperature. In the MGCM simulation of Section 5.2, the SK2 has a peak amplitude in temperature of about 0.5 K. There is little vertical variation in the temperature field at pressures greater than 10 Pa, and the meridional structure is the same as in Fig. 8A. The SK2 mode has so far eluded detection in temperature measurements by the MGS TES (e.g., Banfield et al., 2003).

Withers et al. (2003) explored the behavior of solar-asynchronous tides at altitudes of 130–160 km through analysis and modeling of MGS accelerometer measurements. As in earlier investigations (e.g., Wilson, 2002), they characterized the zonal variations of neutral density within subsets of data at fixed altitude, latitude, and local time, but their results extend to tidal modulation at $f = 4$ sol^{-1}, which had not been considered previously. The $f = 4$ sol^{-1} modulation is strongest in the tropics,

where the normalized amplitude in density approaches 20% at 130 km altitude during mid-to-late spring of MY 24 (Withers et al., 2003, Fig. 8). This is about an order of magnitude larger than the normalized density variations in the lower atmosphere implied by the measurements in Fig. 5.

Withers et al. (2003) used classical tidal theory to model the accelerometer measurements, which led them to conclude that the $f = 4$ sol^{-1} modulation is probably caused by the SK2. [The SK2 corresponds to the "−2,2,2" Hough function of LTE (e.g., Zurek, 1988).] However, subsequent numerical simulations by the MGCM of the Laboratoire de Météorologie Dynamique predict that the DK3 should have a significantly larger amplitude than the SK2 at aerobraking altitudes in the tropics (Angelats i Coll et al., 2004, Figs. 4–5). This result conforms with intuition in that the wave amplitude should grow more rapidly with increasing height for the vertically propagating DK3 than for the vertically evanescent SK2. The MGS accelerometer sampled the tropical atmosphere at only a single local time, so that both modes are consistent with the observations. Hence, the SK2 is probably responsible for some of the $f = 4$ sol^{-1} modulation in the accelerometer measurements, but it may well not be the primary source.

In summary, the SK2 appears to be responsible for distinctive seasonal variations in $S_2(p)$ observed by the Viking Landers (Wilson and Hamilton, 1996; Bridger and Murphy, 1998). The mode is nearly resonant, which enhances its effect on surface pressure (Zurek, 1988). The amplitude of the SK2 in geopotential height grows steadily with decreasing pressure, as shown in Fig. 5A, reaching typical values of about 100 m in the lower atmosphere that are readily detectable in radio occultations. This steady growth in amplitude also results is strong modulation of both geopotential height and neutral density at aerobraking altitudes (Withers et al., 2003; Angelats i Coll et al., 2004).

6. The diurnal Kelvin wave

We now consider the strong spectral feature at $f = 2$ sol^{-1} in Fig. 4A. We will show that it arises from a diurnal Kelvin wave by using the same combination of data analysis and modeling as in the previous section.

6.1. Observations

We used the same subsets of MGS and MEX data and the same method of analysis as described in Section 5.1. Fig. 9 shows the resulting solutions for A and λ_m for the $f = 2$ sol^{-1} mode. As in Fig. 5 we have restricted analysis to pressures less than 400 Pa.

The amplitude of the $f = 2$ sol^{-1} mode generally increases with decreasing pressure, as shown in Fig. 9A, but at a slower rate than expected for a vertically propagating wave. The amplitude tends to be larger in the MEX measurements, which are closer to the equator. At the 200 Pa pressure level, the amplitudes observed by MGS and MEX are 106 ± 6 m and 203 ± 11 m, respectively.

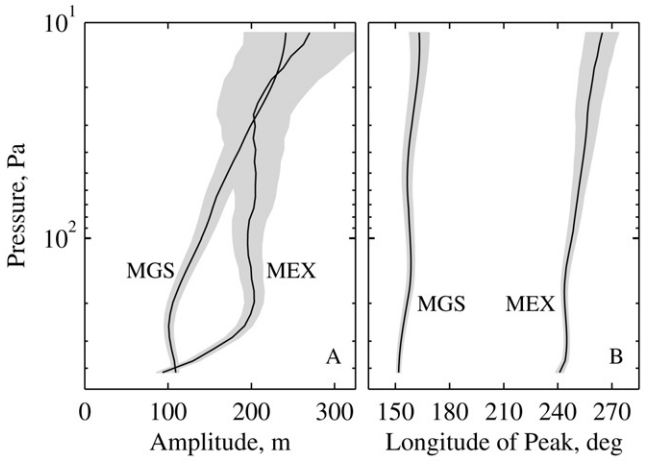

Fig. 9. Structure of the $f = 2$ sol^{-1} wave mode as derived from measurements of geopotential height by MGS and MEX. The dark lines show least squares solutions for (A) the amplitude A and (B) the longitude of maximum geopotential λ_m. The standard deviations are denoted by gray shading. The MGS measurements are at latitude 35° N and local time 4.2 h. The MEX measurements are closer to the equator, centered at 10° N, and roughly half a day later in local time at 17.1 h.

The variation of phase with pressure is similar in both the MGS and MEX observations, as shown in Fig. 9B. In both cases λ_m tilts slightly eastward with increasing height, shifting by about 11° for MGS and about 24° for MEX. When the profiles of λ_m are averaged over pressure, we obtain mean values $\overline{\lambda_m}$ of 158° E at local time 4.2 h (MGS) and 251° E at local time 17.1 h (MEX). When $fT = 2$, the solutions for $\overline{\lambda_m}$ are ambiguous by integer multiples of π radians or 180° of longitude. The change in $\overline{\lambda_m}$ that occurs in the 12.9 h interval in local time between the MGS and MEX observations is therefore

$$\overline{\lambda_m}(17.1\text{ h}) - \overline{\lambda_m}(4.2\text{ h}) = 93° + n \times 180°, \tag{10}$$

where n is any integer. This constraint on the variation of $\overline{\lambda_m}$ with t_L is shown in Fig. 10.

As before, we interpreted this result through use of Eq. (8). Fig. 10 shows the expected variation of λ_m with t_L for several possible combinations of s and σ when $fT = 2$. The eastward traveling, wave-1, diurnal tide ($s = 1$, $\sigma = 1$ sol^{-1}) yields the best fit to the observations, followed closely by the westward traveling, wave-3, diurnal tide. The behavior of the stationary and semidiurnal modes is inconsistent with the measurements.

6.2. MGCM simulations

We now extend our evaluation of the MGCM by testing its performance against the results in Figs. 9 and 10. We applied space–time Fourier analysis to the simulated geopotential field at $L_s = 50°$, searching in this case for atmospheric waves with combinations of s and σ that yield $f = 2$ sol^{-1}, such as those noted in Fig. 10. The dominant mode appearing in the simulation at middle-to-low latitudes and pressures greater than 10 Pa is an eastward-traveling, wave-1, diurnal tide ($s = 1$, $\sigma = 1$ sol^{-1}). A stationary wave ($s = 2$) makes a much smaller

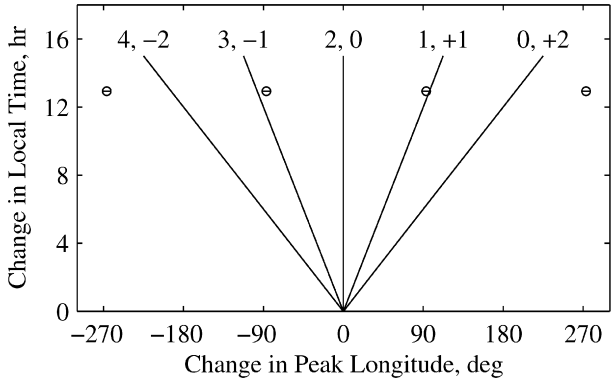

Fig. 10. Variation of λ_m with t_L for the $f = 2\ \mathrm{sol}^{-1}$ wave mode. The circles show results derived from the MGS and MEX observations, as expressed by Eq. (10), with horizontal bars that indicate the standard deviation of the combined measurements. The set of five lines shows the predictions of the simple wave model in Eq. (8). The numbers adjacent to each line indicate the assumed values of s and σ, respectively, with the latter expressed in sol^{-1}. Each combination yields $f = 2\ \mathrm{sol}^{-1}$.

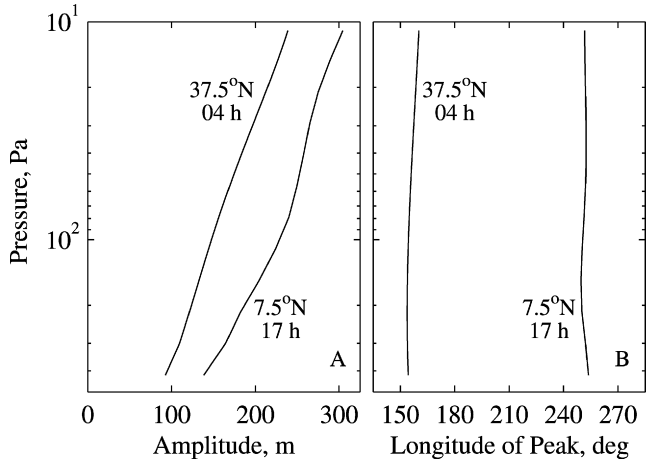

Fig. 11. Structure of the dominant $f = 2\ \mathrm{sol}^{-1}$ wave mode ($s = 1$, $\sigma = 1\ \mathrm{sol}^{-1}$) in the MGCM simulation at $L_s = 50°$. The two panels show vertical profiles of (A) A and (B) λ_m as simulated by the MGCM at essentially the same latitudes and local times as the observations in Fig. 9.

but noteworthy contribution to the geopotential field, particularly in the southern tropics. Within these ranges of pressure and latitude, the amplitudes of all other relevant modes are insignificant. Hence, the MGCM strongly favors the same values for s and σ that yield the best fit to the observations in Fig. 10.

We further characterized the dominant mode in the MGCM simulation ($s = 1, \sigma = 1\ \mathrm{sol}^{-1}$) by calculating its amplitude and phase in geopotential height. Fig. 11 shows the results at essentially the same latitudes and local times as the measurements in Fig. 9. The simulated wave captures the main features of the observations—including the absolute amplitude, the absolute phase, and their vertical variations—with no major discrepancies. The MGCM does a particularly good job of matching the MGS observations at 35° N, confirming the correspondence between the simulated and observed wave modes.

Having validated the simulation against the results in Figs. 9 and 10, we can now use it to deduce the wave's identity and explore other aspects of its behavior. Fig. 12 shows the simulated

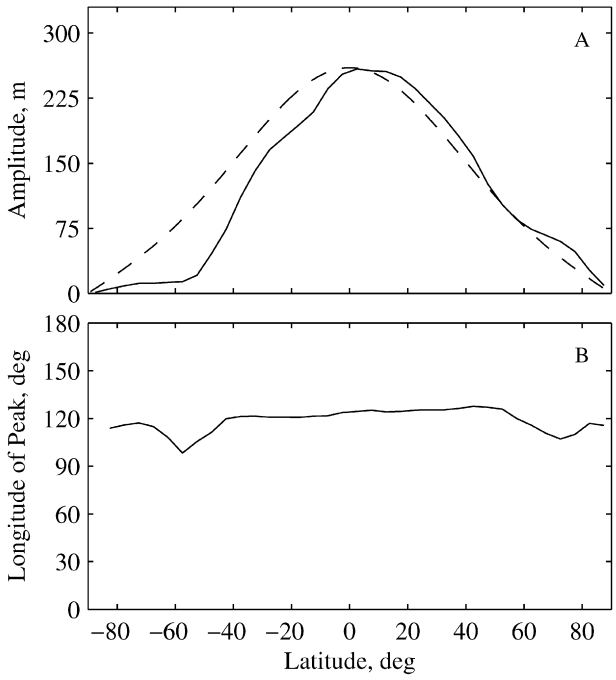

Fig. 12. Numerical models for wave structure at the 43-Pa pressure level. The solid lines show (A) the amplitude in geopotential height and (B) the longitude of the peak in geopotential for the eastward-propagating, wave-1, diurnal tide in the MGCM simulation at $L_s = 50°$. The phase is shown at a local time of 0 h over the latitude range where the amplitude exceeds 2 m. The dashed line in the upper panel shows the meridional structure predicted by Laplace's tidal equations for a diurnal, wave-1, Kelvin wave.

amplitude and phase of the wave at 43 Pa. The mode resembles a Kelvin wave in that the amplitude is roughly symmetric about the equator and decreases steadily from equator to pole with a large meridional scale. At 0 h local time, the peak in the simulated geopotential field occurs at an average longitude of 119° E, and there is little variation of phase with latitude, as shown in Fig. 12B.

Finally, Fig. 12A compares the meridional structure from the MGCM with the predictions of LTE for a diurnal, wave-1, Kelvin wave (DK1). The DK1 has the same zonal phase speed as the SK2, about 240 $\mathrm{m\,s}^{-1}$ at the equator, so that LTE should be reasonably accurate. The results from the two models are generally consistent, reinforcing our conclusion about the wave's identity.

6.3. Discussion

The DK1 is a characteristic feature of the martian atmosphere, imposing a distinctive signature on observations by several instruments. The new results derived here corroborate and extend previous measurements at the surface by the Viking Landers, in the lower atmosphere by the MGS TES, and at aerobraking altitudes by the MGS accelerometer.

In Section 5.3 we discussed the investigation of $S_2(p)$ by Wilson and Hamilton (1996), which combined MGCM modeling with analysis of Viking Lander pressure measurements. That study also encompassed the diurnal oscillations in surface pressure $S_1(p)$, and we now consider that aspect of their re-

sults. In a suite of simulations with the GFDL MGCM, Wilson and Hamilton (1996) found that zonal variations of topography and surface thermal properties excite a variety of solar-asynchronous tidal modes through modulation of the basic solar-locked components of the tides. The strongest asynchronous mode is a nearly resonant, eastward propagating DK1, confirming previous predictions based on classical tidal theory (Zurek, 1976, 1988; Conrath, 1976). Simulations of $S_1(p)$ contain a prominent standing wave produced by interference between the eastward traveling DK1 and the westward traveling solar-locked diurnal tide ($s = 1$, $\sigma = -1$ sol^{-1}) (Wilson and Hamilton, 1996, Fig. 9a). As a general rule the two modes have similar amplitudes in surface pressure, but the DK1 dominates around northern summer solstice when the mode is closest to resonance (Wilson and Hamilton, 1996, Figs. 10 and 20; Bridger and Murphy, 1998, Fig. 3b). This prediction of a seasonal enhancement in the amplitude of the DK1 is consistent with the anomalously early phase of $S_1(p)$ observed at this season by the Viking Landers. By identifying the signature of the DK1 in the Viking Lander pressure measurements, the MGCM yields strong evidence for its presence in the martian atmosphere.

The DK1 has been observed directly in the lower atmosphere at altitudes of 0–40 km through temperature sounding by the MGS TES (Wilson, 2000; Banfield et al., 2003). Wilson (2000) characterized its behavior during midsummer of the northern hemisphere ($L_s = 120°$–$140°$), supplementing analysis of TES data with modeling by the GFDL MGCM. The DK1 has a peak amplitude at the 50-Pa pressure level of about 1.5 K, and its meridional structure is essentially the same as in Fig. 12 (Wilson, 2000, Fig. 2a). Banfield et al. (2003) later conducted a far more comprehensive investigation of forced waves through analysis of TES nadir temperature retrievals. This effort yielded the most extensive characterization to date of stationary waves on Mars. They also examined a variety of tidal modes including the DK1, mapping its global structure and seasonal variations during a full martian year (Banfield et al., 2003, Fig. 11). The DK1 persists throughout the year with a typical amplitude of 1–2 K within the tropics. The variations of phase with latitude, altitude, and season are relatively small.

The vertical structure of the DK1 is nearly evanescent, and its amplitude in geopotential grows steadily with increasing height (Figs. 9 and 11). This growth extends to aerobraking altitudes (110–160 km) where the DK1 imposed strong zonal modulation on measurements of neutral density by the MGS accelerometer (Forbes and Hagan, 2000). Wilson (2002) and Withers et al. (2003) characterized its structure through analysis of accelerometer data from mid-to-late spring of MY 24, roughly the same season as the occultation data considered here. The meridional structure of the DK1 is broad and roughly symmetric about the equator, as in Fig. 12, with a peak amplitude in density of about 25% at 130 km altitude (Wilson, 2002; Withers et al., 2003). According to the measurements in Fig. 9, the corresponding density variations in the lower atmosphere are smaller by about an order of magnitude.

In summary, the DK1 has been observed through pressure measurements by the Viking Landers, through temperature sounding by the MGS TES, through measurements of neutral density by the MGS accelerometer, and now through measurements of geopotential height in radio occultations. It is difficult to compare these results directly, owing to differences in the time of observation, the altitude range of the data, and the quantity being measured. However, the GFDL MGCM has been reasonably successful in simulating each set of measurements (Wilson and Hamilton, 1996; Wilson, 2000, 2002), demonstrating that the data are mutually consistent to a significant degree.

7. Conclusions

This paper reports new observations and numerical simulations of Kelvin waves on Mars. We retrieved atmospheric profiles from a series of radio occultation experiments conducted with MEX and MGS in mid-2004, and we used the results to characterize the geopotential field of Mars. These data reveal strong modulation from solar-asynchronous thermal tides (Fig. 4A). We determined the zonal and vertical structure of two prominent tidal modes through least-squares analysis of the geopotential measurements (Figs. 5 and 9). We then deduced the period and zonal wave number of both modes (Figs. 6 and 10) by exploiting the complementary coverage of the MEX and MGS observations in local time. A numerical simulation by the GFDL MGCM was successful in reproducing the main features of the observations (Figs. 3, 7, and 11). The results derived from the validated simulation allow both the SK2 and the DK1 to be identified with confidence. This combination of measurements and modeling yields important new insight, particularly for the SK2 where few other observations are currently available (Section 5.3). For the DK1, our results are generally consistent with previous observations by diverse instruments (Section 6.3), confirming the reliability of our data and method of analysis.

Both the DK1 and the SK2 will influence the design of future missions to Mars. Their effect on aerobraking was discussed already in Sections 5.3 and 6.3. In addition, both tidal modes produce significant modulation of surface pressure (Zurek, 1988; Wilson and Hamilton, 1996; Bridger and Murphy, 1998), with implications for attempts to land spacecraft on the surface, and we now briefly discuss this aspect of their behavior.

Fig. 13 shows how the surface pressure at 2.5° N varies with longitude and local time in the simulation by the GFDL MGCM. We applied space–time spectral analysis and found that four tidal modes are responsible for most of the variations in surface pressure. These are the solar-locked diurnal tide, with an amplitude of 1.1%, the DK1 (1.5%), the solar-locked semidiurnal tide (0.7%), and the SK2 (0.4%). When displayed in this way, the modulation of surface pressure by the solar-locked tides is independent of longitude, while both the DK1 and the SK2 produce a pattern of modulation that drifts steadily eastward by 180° per sol (see Figs. 6 and 10). Interference among these four modes produces a complicated pattern of variations in surface pressure, as shown in Fig. 13A. The magnitude of the daily fluctuations depends strongly on longitude, with excursions as large as +3.9% and −3.5% at 189° E and as small

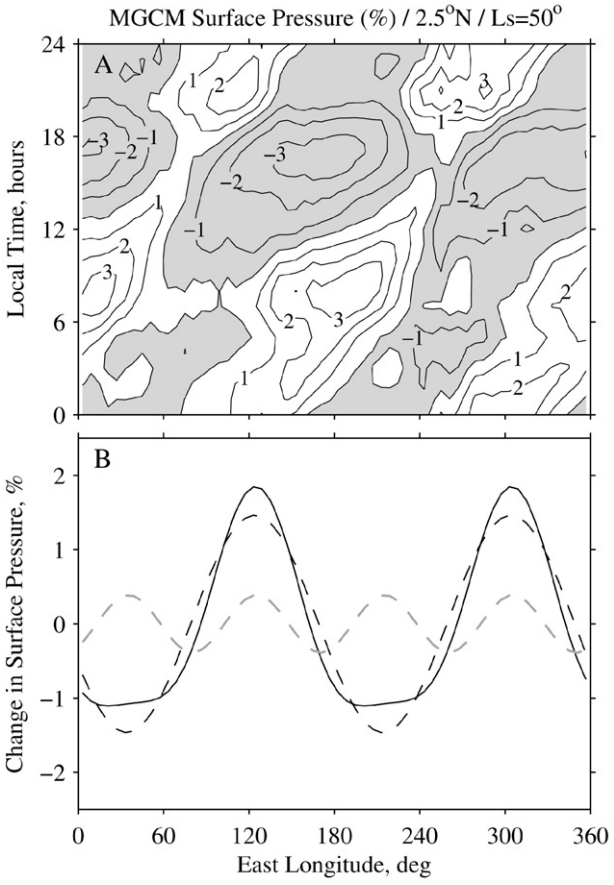

Fig. 13. (A) Variations of surface pressure with longitude and local time in the MGCM simulation. Results are shown at 2.5° N for $L_s = 50°$. The pressure variations are expressed as a percentage of the daily average at each longitude. The contour interval is 1%. (B) Contributions by Kelvin waves to the simulated surface pressure field at local time 0 h. The combination of the DK1 (dark dashed line) and the SK2 (light dashed line) produces net modulation (solid line) with relatively narrow peaks and broad troughs.

as +0.7% and −0.6% at 63° E. The local times of the maxima and minima also vary strongly with longitude.

Fig. 13B illustrates the relative phase of the DK1 and the SK2, which plays an important role in shaping the pressure field at the surface. The superposition of these two Kelvin waves results in pressure peaks that are intense (1.9%) and relatively narrow, while the pressure troughs are shallow (1.1%) and relatively broad.

As noted in Section 5.2, the GFDL MGCM appears to underestimate the amplitude of the SK2 by about a factor of two at $L_s = 50°$. We explored one possible explanation for this discrepancy by conducting supplementary simulations that include the radiative effects of water ice clouds (cf. Hinson and Wilson, 2004). The SK2 has a significantly stronger amplitude than in the cloud-free simulation, resulting in closer agreement with the observations, but the physical mechanism behind this intensification of the SK2 is not understood at present. This is an interesting topic for future research. At the same time, we plan to analyze a broader set of radio occultation measurements to characterize the seasonal variations of the DK1 and the SK2, including their response to dust storms. The results should provide additional challenges for MGCM modeling.

Acknowledgments

We are indebted to R. Simpson and J. Twicken for their contributions to experiment operations, data management, and data reduction. We are forever grateful to S. Asmar and the Radio Science Systems Group at JPL for their nearly flawless performance in acquiring data with the radio science receivers at the DSN complexes. This work has made use of NASA's Navigation and Ancillary Information Facility (Acton, 1996) and the Smithsonian/NASA Astrophysics Data System (http://adswww.harvard.edu/). The manuscript was prepared with an Icarus LaTeX template created by R.A. Beyer, D.P. O'Brien, P. Withers, and G. Bart (http://rossbeyer.net/software/). The work at Universität der Bundeswehr München was supported by BMWT under DLR grant 50-QM-0401. The work at Stanford University was made possible through funding from NASA that supports the radio science investigations of both MGS and MEX.

References

Acton, C.H., 1996. Ancillary data services of NASA's navigation and ancillary information facility. Planet. Space Sci. 44, 65–70.

Andrews, D.G., Holton, J.R., Leovy, C.B., 1987. Middle Atmosphere Dynamics. Elsevier, New York.

Angelats i Coll, M., Forget, F., López-Valverde, M.A., Read, P.L., Lewis, S.R., 2004. Upper atmosphere of Mars up to 120 km: Mars Global Surveyor accelerometer data analysis with the LMD general circulation model. J. Geophys. Res. (Planets) 109, doi:10.1029/2003JE002163. E01011.

Banfield, D., Conrath, B., Pearl, J.C., Smith, M.D., Christensen, P., 2000. Thermal tides and stationary waves on Mars as revealed by Mars Global Surveyor thermal emission spectrometer. J. Geophys. Res. (Planets) 105, 9521–9538, doi:10.1029/1999JE001161.

Banfield, D., Conrath, B.J., Smith, M.D., Christensen, P.R., Wilson, R.J., 2003. Forced waves in the martian atmosphere from MGS TES nadir data. Icarus 161, 319–345.

Bougher, S.W., Engel, S., Hinson, D.P., Forbes, J.M., 2001. Mars Global Surveyor Radio Science electron density profiles: Neutral atmosphere implications. Geophys. Res. Lett. 28, 3091–3094, doi:10.1029/2001GL012884.

Bridger, A.F.C., Murphy, J.R., 1998. Mars' surface pressure tides and their behavior during global dust storms. J. Geophys. Res. (Planets) 103, 8587–8602, doi:10.1029/98JE00242.

Cahoy, K.L., Hinson, D.P., Tyler, G.L., 2006. Radio science measurements of atmospheric refractivity with Mars Global Surveyor. J. Geophys. Res. (Planets) 111, doi:10.1029/2005JE002634. E05003.

Chapman, W.A., Cross, M.J., Flower, D.A., Peckham, G.E., Smith, S.D., 1974. A spectral analysis of global atmospheric temperature fields observed by the Selective Chopper Radiometer on the Nimbus 4 satellite during the year 1970–1. Proc. R. Soc. London Ser. A 338, 57–76.

Clancy, R.T., Wolff, M.J., Christensen, P.R., 2003. Mars aerosol studies with the MGS TES emission phase function observations: Optical depths, particle sizes, and ice cloud types versus latitude and solar longitude. J. Geophys. Res. (Planets) 108 (E9), doi:10.1029/2003JE002058. 5098.

Conrath, B.J., 1976. Influence of planetary-scale topography on the diurnal thermal tide during the 1971 martian dust storm. J. Atmos. Sci. 33, 2430–2439.

Conrath, B.J., 1981. Planetary-scale wave structure in the martian atmosphere. Icarus 48, 246–255.

Fjeldbo, G., Kliore, A.J., Eshleman, V.R., 1971. The neutral atmosphere of Venus as studied with the Mariner V radio occultation experiments. Astron. J. 76, 123–140.

Forbes, J.M., Hagan, M.E., 2000. Diurnal Kelvin wave in the atmosphere of Mars: Towards an understanding of 'stationary' density structures observed by the MGS accelerometer. Geophys. Res. Lett. 27, 3563–3566, doi:10.1029/2000GL011850.

Hinson, D.P., 2006. Radio occultation measurements of transient eddies in the northern hemisphere of Mars. J. Geophys. Res. (Planets) 111, doi:10.1029/2005JE002612. E05002.

Hinson, D.P., Wilson, R.J., 2002. Transient eddies in the southern hemisphere of Mars. Geophys. Res. Lett. 29 (7), doi:10.1029/2001GL014103. 1154.

Hinson, D.P., Wilson, R.J., 2004. Temperature inversions, thermal tides, and water ice clouds in the martian tropics. J. Geophys. Res. (Planets) 109, doi:10.1029/2003JE002129. E01002.

Hinson, D.P., Simpson, R.A., Twicken, J.D., Tyler, G.L., Flasar, F.M., 1999. Initial results from radio occultation measurements with Mars Global Surveyor. J. Geophys. Res. (Planets) 104, 26997–27012.

Hinson, D.P., Wilson, R.J., Smith, M.D., Conrath, B.J., 2003. Stationary planetary waves in the atmosphere of Mars during southern winter. J. Geophys. Res. (Planets) 108 (E1), doi:10.1029/2002JE001949. 5004.

Jenkins, J.M., Steffes, P.G., Hinson, D.P., Twicken, J.D., Tyler, G.L., 1994. Radio occultation studies of the Venus atmosphere with the Magellan spacecraft. 2. Results from the October 1991 experiments. Icarus 110, 79–94.

Karayel, E.T., Hinson, D.P., 1997. Sub-Fresnel-scale vertical resolution in atmospheric profiles from radio occultation. Radio Sci. 32, 411–424.

Lait, L.R., Stanford, J.L., 1988. Applications of asynoptic space–time Fourier transform methods to scanning satellite measurements. J. Atmos. Sci. 45, 3784–3799.

Lemoine, F.G., Smith, D.E., Rowlands, D.D., Zuber, M.T., Neumann, G.A., Chinn, D.S., Pavlis, D.E., 2001. An improved solution of the gravity field of Mars (GMM-2B) from Mars Global Surveyor. J. Geophys. Res. (Planets) 106, 23359–23376.

Leovy, C.B., 1981. Observations of martian tides over two annual cycles. J. Atmos. Sci. 38, 30–39.

Montmessin, F., Forget, F., Rannou, P., Cabane, M., Haberle, R.M., 2004. Origin and role of water ice clouds in the martian water cycle as inferred from a general circulation model. J. Geophys. Res. (Planets) 109, doi:10.1029/2004JE002284. 10004.

Pätzold, M., Neubauer, F.M., Carone, L., Hagermann, A., Stanzel, C., Häusler, B., Remus, S., Selle, J., Hagl, D., Hinson, D.P., Simpson, R.A., Tyler, G.L., Asmar, S.W., Axford, W.I., Hagfors, T., Barriot, J.-P., Cerisier, J.-C., Imamura, T., Oyama, K.-I., Janle, P., Kirchengast, G., Dehant, V., 2004. MaRS: Mars Express Orbiter Radio Science. In: Mars Express: The Scientific Payload, ESA SP-1240. European Space Research and Technology Centre, Noordwijk, pp. 141–163.

Putzig, N.E., Mellon, M.T., Kretke, K.A., Arvidson, R.E., 2005. Global thermal inertia and surface properties of Mars from the MGS mapping mission. Icarus 173, 325–341.

Salby, M.L., 1982. Sampling theory for asynoptic satellite observations. Part I. Space–time spectra, resolution, and aliasing. J. Atmos. Sci. 39, 2577–2600.

Smith, D.E., Zuber, M.T., Frey, H.V., Garvin, J.B., Head, J.W., Muhleman, D.O., Pettengill, G.H., Phillips, R.J., Solomon, S.C., Zwally, H.J., Banerdt, W.B., Duxbury, T.C., Golombek, M.P., Lemoine, F.G., Neumann, G.A., Rowlands, D.D., Aharonson, O., Ford, P.G., Ivanov, A.B., Johnson, C.L., McGovern, P.J., Abshire, J.B., Afzal, R.S., Sun, X., 2001. Mars Orbiter Laser Altimeter: Experiment summary after the first year of global mapping of Mars. J. Geophys. Res. (Planets) 106, 23689–23722, doi:10.1029/2000JE001364.

Smith, M.D., 2004. Interannual variability in TES atmospheric observations of Mars during 1999–2003. Icarus 167, 148–165.

Tyler, G.L., Balmino, G., Hinson, D.P., Sjogren, W.L., Smith, D.E., Simpson, R.A., Asmar, S.W., Priest, P., Twicken, J.D., 2001. Radio science observations with Mars Global Surveyor: Orbit insertion through one Mars year in mapping orbit. J. Geophys. Res. (Planets) 106, 23327–23348, doi:10.1029/2000JE001348.

Wang, H., Richardson, M.I., Wilson, R.J., Ingersoll, A.P., Toigo, A.D., Zurek, R.W., 2003. Cyclones, tides, and the origin of a cross-equatorial dust storm on Mars. Geophys. Res. Lett. 30 (9), doi:10.1029/2002GL016828. 1488.

Wang, L., Fritts, D.C., Tolson, R.H., 2006. Nonmigrating tides inferred from the Mars Odyssey and Mars Global Surveyor aerobraking data. Geophys. Res. Lett. 33, doi:10.1029/2006GL027753. L23201.

Wilson, R.J., 2000. Evidence for diurnal period Kelvin waves in the martian atmosphere from Mars Global Surveyor TES data. Geophys. Res. Lett. 27, 3889–3892, doi:10.1029/2000GL012028.

Wilson, R.J., 2002. Evidence for nonmigrating thermal tides in the Mars upper atmosphere from the Mars Global Surveyor Accelerometer Experiment. Geophys. Res. Lett. 29 (7), doi:10.1029/2001GL013975. 1120.

Wilson, R.J., Hamilton, K., 1996. Comprehensive model simulation of thermal tides in the martian atmosphere. J. Atmos. Sci. 53, 1290–1326.

Wilson, R.J., Banfield, D., Conrath, B.J., Smith, M.D., 2002. Traveling waves in the Northern Hemisphere of Mars. Geophys. Res. Lett. 29 (14), doi:10.1029/2002GL014866. 1684.

Withers, P., Bougher, S.W., Keating, G.M., 2003. The effects of topographically-controlled thermal tides in the martian upper atmosphere as seen by the MGS accelerometer. Icarus 164, 14–32.

Wolff, M.J., Clancy, R.T., 2003. Constraints on the size of martian aerosols from Thermal Emission Spectrometer observations. J. Geophys. Res. (Planets) 108 (E9), doi:10.1029/2003JE002057. 5097.

Zurek, R.W., 1976. Diurnal tide in the martian atmosphere. J. Atmos. Sci. 33, 321–337.

Zurek, R.W., 1988. Free and forced modes in the martian atmosphere. J. Geophys. Res. (Planets) 93, 9452–9462.

Zurek, R.W., Leovy, C.B., 1981. Thermal tides in the dusty martian atmosphere—A verification of theory. Science 213, 437–439.

Zurek, R.W., Barnes, J.R., Haberle, R.M., Pollack, J.B., Tillman, J.E., Leovy, C.B., 1992. Dynamics of the atmosphere of Mars. In: Kieffer, H.H., Jakosky, B.M., Snyder, C.W., Matthews, M.S. (Eds.), Mars. Univ. of Arizona Press, Tucson, pp. 835–933.